The Astrophysical Journal Letters, 930:L26 (12pp), 2022 May 10 https://doi.org/10.3847/2041-8213/ac66ce


# Water UV-shielding in the Terrestrial Planet-forming Zone: Implications from Water Emission

Arthur D. Bosman, Edwin A. Bergin, Jenny Calahan, and Sara E. Duval
University of Michigan, LSA Astronomy, 1085 S University, Ann Arbor, MI 48109, USA; arbos@umich.edu
*Received 2022 February 17; revised 2022 April 4; accepted 2022 April 12; published 2022 May 16*

## Abstract

Mid-infrared spectroscopy is one of the few ways to observe the composition of the terrestrial planet-forming zone, the inner few astronomical units, of protoplanetary disks. The species currently detected in the disk atmosphere, for example, CO, $CO_2$, $H_2O$, and $C_2H_2$, are theoretically enough to constrain the C/O ratio on the disk surface. However, thermochemical models have difficulties in reproducing the full array of detected species in the mid-infrared simultaneously. In an effort to get closer to the observed spectra, we have included water UV-shielding as well as more efficient chemical heating into the thermochemical code Dust and Lines. We find that both are required to match the observed emission spectrum. Efficient chemical heating, in addition to traditional heating from UV photons, is necessary to elevate the temperature of the water-emitting layer to match the observed excitation temperature of water. We find that water UV-shielding stops UV photons from reaching deep into the disk, cooling down the lower layers with a higher column. These two effects create a hot emitting layer of water with a column of 1–10 $\times$ $10^{18}$ $cm^{-2}$. This is only 1%–10% of the water column above the dust $\tau = 1$ surface at mid-infrared wavelengths in the models and represents <1% of the total water column.

*Unified Astronomy Thesaurus concepts:* Astrochemistry (75); Protoplanetary disks (1300)

## 1. Introduction

The Spitzer Space Telescope has revealed that the inner ~1 au of most protoplanetary disks is rich in water and small organic molecules (e.g., Carr & Najita 2008; Salyk et al. 2011; Pontoppidan et al. 2014). It is within this same 1 au of the star that a significant amount of the best-studied exoplanets currently reside (e.g., Madhusudhan 2019; Fulton et al. 2021). Depending on whether the planets migrated to their current location or if they formed locally, there must be a strong connection between the gas observed in the mid-infrared with the composition of these inner planets.

To fully exploit this connection and possibly unravel the formation origin of these inner planets, the elemental composition of the inner disk gas needs to be measured. After more than a decade of efforts on both the modeling and observational side, it is still unclear how to extract the elemental composition from the mid-infrared spectral information. The main carbon and oxygen carriers, CO, $CO_2$, and $H_2O$, can be observed in the infrared and so C/O ratios should be readily attainable (Najita et al. 2003; Carr & Najita 2008; Pontoppidan et al. 2010; Salyk et al. 2011; Brown et al. 2013). However, due to uncertainties associated with extracting accurate column densities from emission, it is difficult to derive accurate C/O ratios. Observations show that $CO_2$ is not a dominant carrier of either carbon or oxygen (Pontoppidan & Blevins 2014; Bosman et al. 2017). Detailed models of water get stuck on a degeneracy between gas-to-dust abundance and water abundance (Meijerink et al. 2009; Blevins et al. 2016), whereas models of the CO rovibrational lines are very sensitive to the assumed structures (Bosman et al. 2019; Antonellini et al. 2020). As such, C/O ratios have only been inferred from infrared data in TW Hya, where $H_2$ lines are available to infer the total column and the inner disk structure can be resolved (Bosman & Banzatti 2019).

An additional problem for extracting column densities from the observations is that the inferred column density from 2D thermochemical models and 1D slab models when reproducing the same spectra can differ by orders of magnitude. For water, this disparity is best illustrated by comparing Meijerink et al. (2009) and Salyk et al. (2011). The 2D models from Meijerink et al. (2009) predict $H_2O$ that columns of $\gtrsim 10^{20}$ $cm^{-2}$ above the dust photosphere are necessary to reproduce the Spitzer-IRS water spectra, while slab model analysis from Salyk et al. (2011) finds most disks have water columns between $10^{18}$ and $10^{19}$ $cm^{-2}$. More recent modeling efforts support the Meijerink et al. (2009) result of high $H_2O$ columns above the dust photosphere (Blevins et al. 2016; Woitke et al. 2019). Similar column discrepancies between the slab and 2D models are also seen for HCN (Bruderer et al. 2015) and $CO_2$ (Bosman et al. 2017). This uncertainty in the conversion of the observed molecular column makes it difficult to properly anchor any attempt at extracting C/O ratios directly from the column densities of CO and $H_2O$.

Modeling studies have shown that the composition of gas within the inner disk is dependent on the elemental composition, specifically the C/O ratio (Woitke et al. 2019; Anderson et al. 2021). This could allow for a C/O ratio measurement that is independent of the absolute column of $H_2O$. However, current models cannot simultaneously match $H_2O$, $CO_2$, and $C_2H_2$, the three species most sensitive to the C/O ratio. This indicates that current models are missing part of the thermochemical puzzle. In particular, the effects of water UV-shielding have been shown to be present (Bethell & Bergin 2009) but are not widely included in modeling efforts. Furthermore, excess heating of the gas is often invoked (e.g., Glassgold et al. 2009; Meijerink et al. 2009; Glassgold & Najita 2015; Anderson et al. 2021) but seldom consistently

include a full thermochemical model. In particular, the models of Ádámkovics et al. (2014, 2016) do include these effects. However, they assumed a gas-to-dust ratio of 100 in disk surface layers, which would not allow for the high $H_2O$ columns inferred from the infrared spectra (Meijerink et al. 2009; Blevins et al. 2016; Woitke et al. 2019). As a result, it is unclear if these models would reproduce the observed emission.

This paper is the first in a series of four (Bosman et al. 2022 ; Calahan et al. 2022; S. E. Duval et al. 2022, in preparation) that explores these issues and presents a way forward for the interpretation of infrared spectral data. The current paper will focus on water itself, using a state-of-the-art thermochemical model to investigate the effects of additional heating as well as water UV-shielding on the predicted water spectra. Future papers will focus on the $CO_2$–$H_2O$ ratios (Bosman et al. 2022), Ly$\alpha$ and $H_2^{18}O$ (Calahan et al. 2022), and organics (Duval et al. 2022, in preparation).

**Table 1**
Model Parameters

| Parameter | Symbol | Value |
|---|---|---|
| Stellar luminosity | | 1 $L_\odot$ |
| Stellar spectrum | | AS 209[a] |
| Stellar mass | | 1.0$M_\odot$ |
| Sublimation radius | $R_{\rm subl}$ | 0.08 au |
| Critical radius | $R_c$ | 46 au |
| Disk outer radius | $R_{\rm out}$ | 100.0 au |
| Gas surf. dens. at $R_c$ | $\Sigma_c$ | 21.32 g cm$^{-2}$ |
| Surf. dens. power-law slope | $\gamma$ | 0.9 |
| Disk opening angle | $h_c$ | [0.08, 0.16] |
| Disk flaring angle | $\psi$ | 0.11 |
| Large dust fraction | | [0.99, 0.999] |
| Large dust settling | $h_d/h_g$ | 0.2 |

**Note.**
[a] Zhang et al. (2021).

## 2. Methods

Our models are based on the Dust and Lines (DALI) code (Bruderer et al. 2012; Bruderer 2013). With a number of extensions to better model the hot inner regions of the disk. The chemical network has been expanded in two ways: by increasing the formation of $H_2$ and including water UV-shielding.

As noted by Glassgold et al. (2009), the presence of water vapor in the warm to hot (∼few hundred K to 1000 K) disk atmosphere requires the a priori presence of $H_2$. Thus, in our model, we have updated the chemistry, especially the formation of $H_2$, as described in Appendix A. Specifically, three-body formation reactions have been added, and $H_2$ formation on grains at temperatures between 300 and 900 K has been increased in line with experiments (Cazaux & Tielens 2002, 2004; Wakelam et al. 2017, see also Thi et al. 2020).

The inferred $H_2O$ columns ($>10^{18}$ cm$^{-2}$) with Spitzer-IRS imply that enough $H_2O$ exists in the inner disk to contribute significantly to the UV opacity of the inner disk gas as noted by Bethell & Bergin (2009). Therefore, we include shielding of UV photons by $H_2O$ (using cross sections from Chan et al. 1993; Fillion et al. 2003, 2004; Mota et al. 2005; Heays et al. 2017). We include the effect of $H_2O$ on the UV flux propagation as a vertical extinction term during the chemistry and thermal balance. As such, we do not just include a self-shielding term, as is common for line-dominated species such as CO, $N_2$, and $H_2$, but a full UV-shielding term, which impacts the dissociation rate of all species as well as the amount of energy injected into the gas by UV photons. The $H_2O$ cross section is averaged within the wavelength bins used during the calculation and the UV flux in the cell is updated based on the $H_2O$ column above the cell.

To be able to self-consistently test the effect of additional heating on the chemistry and line emission, we examine two gas heating formalisms: the standard DALI heating (Bruderer et al. 2012; Bruderer 2013) and extra chemical heating due to photodissociation and molecule formation, following the high-density results from Glassgold & Najita (2015).

The physical model is a smooth version of the AS 209 model from Zhang et al. (2021). The disk parameters are given in Table 1. The stellar input spectrum is also taken from Zhang et al. (2021) and is the combination of a stellar atmosphere model (Nextgen; Hauschildt et al. 1999) and excess UV (Herczeg et al. 2004; Dionatos et al. 2019), which is dominated by Ly$\alpha$ emission, consistent with observations (Schindhelm et al. 2012). The final stellar spectrum is spectral type K5 (4300 K) with a total luminosity of 1.4 $L_\odot$ and 0.01 $L_\odot$ in UV at wavelengths smaller than 200 nm. AS 209 has been chosen as a base model, as its accretion rate of $10^{-7.5}$ $M_\odot$ yr$^{-1}$ creates a more typical stellar irradiation environment than an AS 205N–inspired model (high UV; e.g., Bruderer et al. 2015; Bosman et al. 2017) or TW Hya–inspired model (low UV; Woitke et al. 2018; Anderson et al. 2021). The disk mass in the model, 0.0045 $M_\odot$, is also more typical than the $\gtrsim$0.01 $M_\odot$ disk masses of the aforementioned studies (e.g., van Terwisga et al. 2022).

As the physical structure is very thin, with a scale height of 0.05 at 1 au ($h_c = 0.08$), we have also included a thick model with larger vertical distribution, yielding a scale height of 0.1 at 1 au ($h_c = 0.16$). Most of the dust is assumed to be large dust settled toward the midplane, yielding gas-to-dust ratios in the surface layers of $10^4$ (99% large, settled dust) and $10^5$ (99.9% large, settled dust). Whereas many previous studies have assumed large grains (up to 1 mm) (e.g., Bruderer et al. 2015; Bosman et al. 2017; Woitke et al. 2018), we only use small grains (up to 1 $\mu$m) in the inner disk surface. Dust opacities are calculated using the DSHARP dust opacity tool (Birnstiel et al. 2018) and are the same as the ones used in Zhang et al. (2021).

The water emission lines are calculated using the molecular data file from the Leiden Atomic and Molecular Database. Levels with energies up to 7200 K are included (Tennyson et al. 2001). Line transitions are taken from the BT2 list (Barber et al. 2006) and the collisional rate coefficients are from Faure & Josselin (2008). The water spectra are calculated from the non-LTE level populations using the "fast line ray tracer" as described in Bosman et al. (2017, Appendix B).

To see how our models compare with observations, we create a representative slab model using the parameters in Salyk et al. (2011). We use a water excitation temperature of 500 K and a water column of $3 \times 10^{18}$ cm$^{-2}$. The spectra are calculated using the slab model from Banzatti et al. (2012). Finally, the spectrum is scaled to have the same emitting area as the model with both water UV-shielding and extra chemical heating.

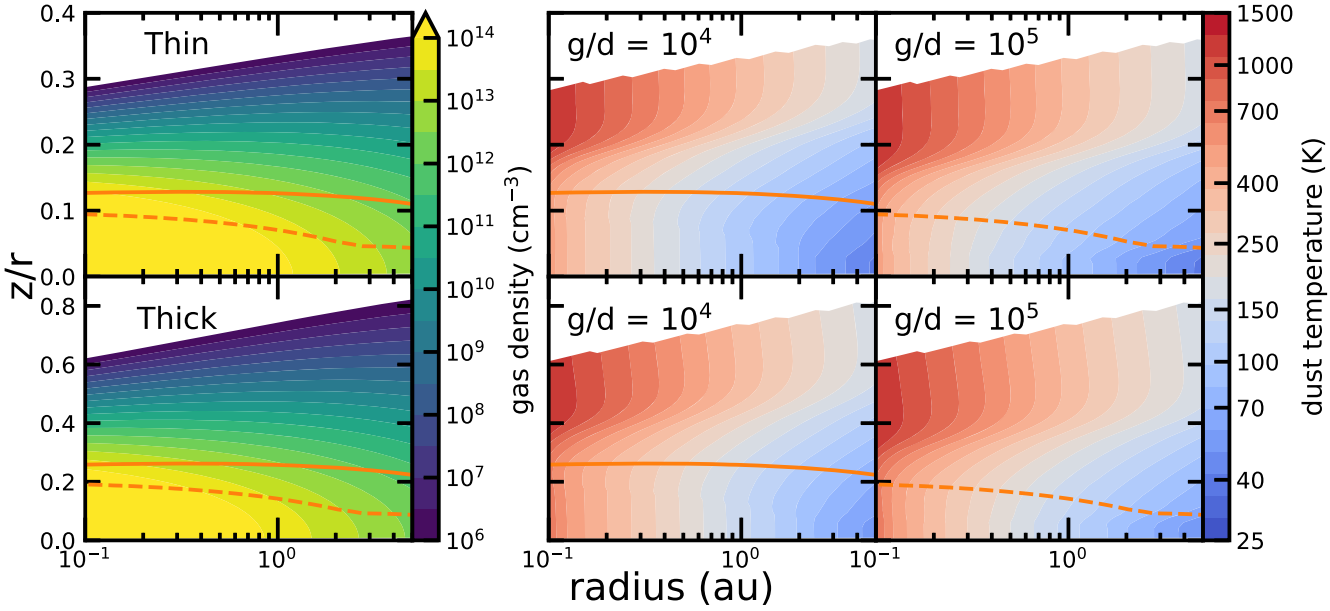


**Figure 1.** Gas density (left) and dust temperature (right) for the different gas and dust structures. The top row shows the thin model ($h_c = 0.08$), and the bottom row shows the thick model ($h_c = 0.16$). The gas-to-dust ratio in the surface layers after settling the large dust is denoted in the top left of the dust temperature panels. Orange lines show the continuum $\tau = 1$ line at 15 $\mu$m for the $g/d = 10^4$ (solid) and $10^5$ (dashed) dust distributions.

## 3. Results

### 3.1. Temperature Structure

Figure 1 shows the gas density and dust temperature for the four different gas and dust structures. The thin models are generally cooler than the thick models near the midplane. This difference disappears in the upper layers where the unattenuated stellar radiation field dictates the dust temperature. The models with a larger surface layer gas-to-dust ratio are also slightly cooler in the midplane as heat escapes more easily in the vertical direction. The larger surface layer gas-to-dust ratio also pushes down the vertical temperature transition, between the heated surface layer and the midplane. This is a result of lower continuum opacities at all wavelengths.

Figure 2 presents the gas-temperature structure for the thin model with a gas-to-dust ratio of $10^5$ in the disk surface for four different thermochemical iterations: standard model (DALI std), standard model with water UV-shielding ($H_2O$ shielding), standard model with chemical heating (chem. heat.), and standard model with both water UV-shielding and chemical heating ($H_2O$ shielding, chem. heat). Appendix B discusses the effect of the different structures. The general behavior seen in Figure 2 is also seen in the other models.

In general, around the location of the dust temperature transition from the heated surface to close to the midplane temperature is where gas and dust become strongly coupled. Above this vertical point ($z/r \gtrsim 0.15$) is where gas and dust are thermally decoupled and where changes in the thermochemistry lead to changes in the gas temperature.

A small effect of water UV-shielding can be seen in the difference between the models with and without water UV-shielding between a $z/r$ of 0.15 and 0.2 (white box in Figure 2). The water UV-shielding models have lower gas temperatures in this region as fewer UV photons reach this layer. This provides less heating of the gas as a result of photodissociation and molecular formation. When extra chemical heating following photodissociation is included, the molecular layer at $z/r \sim 0.15$–$0.2$ is significantly heated, nearly doubling in gas temperature. This region is significantly larger in the case where water UV-shielding is not included. This region is fully molecular and will therefore have a significant impact on the resulting emission-line spectra.

### 3.2. Water Abundance

Figure 2 also provides the water vapor abundance structure for the thin model with a gas-to-dust ratio of $10^5$ on the disk surface for the same four different thermochemical iterations. Different choices in the thermochemical model have strong implications for the water abundance structure. The base DALI model shows a gap in the $H_2O$ abundance between a $z/r$ of 0.1 and 0.15. In this relatively cold gas, <500 K, the formation of OH from $O + H_2$ is very slow. This allows the attenuated UV field in this region to keep a large fraction of the oxygen in atomic form.

This low water abundance region is no longer present when the UV-shielding of water is included. The self-shielding effect filters out all the $H_2O$ dissociating photons in surface layers allowing $H_2O$ to survive in the deeper, colder layers. There now exists a very sharp drop in the $H_2O$ abundance around 0.6 au when the surface layer is not warm enough to efficiently form water and no shielding layer exists. Outside this point, most of the oxygen in the model is in atomic form. When the dust becomes cold enough for water to freeze out, water ice dominates the oxygen budget. Additional chemical heating has little effect on the water vapor abundance. However, the higher gas temperature produced on the surface extends the water-rich layer outward.

### 3.3. Water Spectra

Figure 3 shows the water spectra over the MIRI range compared to a typical slab model (Salyk et al. 2011). The slab model is the best fit to the observed Spitzer/IRS water spectrum and thus is an effective reproduction of the observed water emission. In most of the 10–28 $\mu$m range, our models without additional heating underestimate the line flux. This is

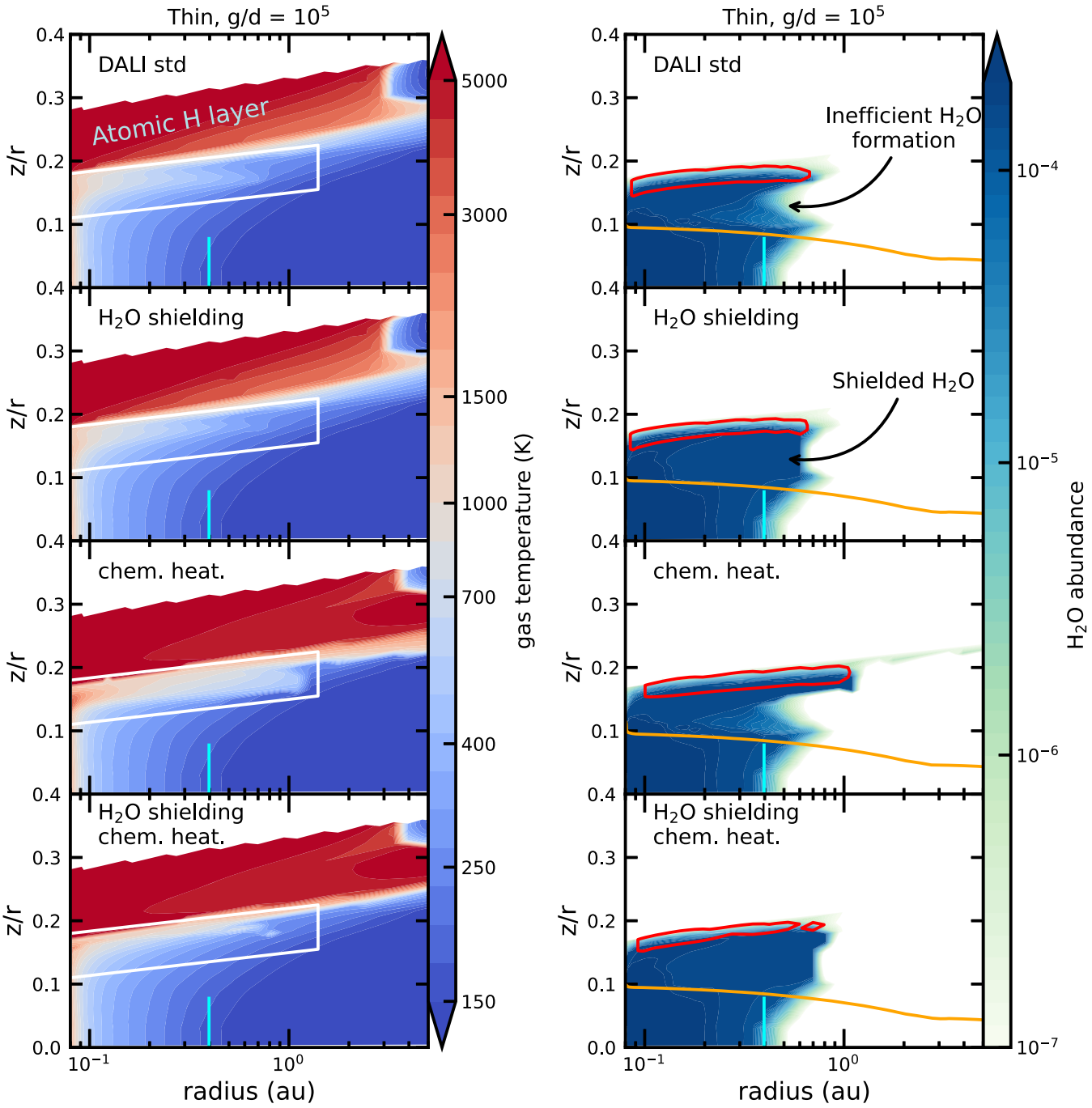


**Figure 2.** Gas temperature (left) and water abundance (right) for the thin model with a surface layer gas-to-dust ratio of $10^5$ for variations in the chemical and heating–cooling models. The vertical blue lines show the midplane $H_2O$ snow-line location in the model. Above a $z/r$ of ∼0.2, hydrogen is dominantly in atomic form and the gas is hot (>1000 K). Below this, models show a warm layer where the gas and dust temperatures are strongly decoupled, but the gas is molecular (region enclosed in the white box). This layer is critical for the inner disk emission. The gas in this layer is heated by UV photons, as such, water UV-shielding cools down this layer, while extra chemical heating leads to higher temperatures. In the right panels, the orange line shows the continuum $\tau = 1$ line at 17 $\mu$m, and the red contours show the origin of 90% of the $11_{3,9}$–$10_{0,10}$ 17.2 $\mu$m water-line flux. Including the effect of water UV-shielding strongly increases the abundance of $H_2O$ between a $z/r$ of 0.1 and 0.15 at radii >0.3 au.

the case even though the emitting area is the same for the slab and 2D model; this indicates that higher temperatures are necessary. Including chemical heating without water UV-shielding creates a spectrum that is very bright due to the gas heating over a large column. The inclusion of water UV-shielding confines the heating to a thin column, and the results are a good match to the slab spectrum.

We note that the brightness ratio between shorter-wavelength flux and longer-wavelength flux for the pure rotational lines is always higher in the DALI models compared to the slab models. Interestingly when comparing the vibrational 6.5 $\mu$m feature and the 10–28 $\mu$m rotational lines, the opposite relation is seen. From the comparison between the slab model and the DALI model spectrum at around 11 $\mu$m, it would be expected that the DALI 6.5 $\mu$m feature would be brighter in all DALI models. This is only seen in the chemical heating model without water UV-shielding, which, as already discussed, is way too bright in the longer wavelengths as well. This indicates

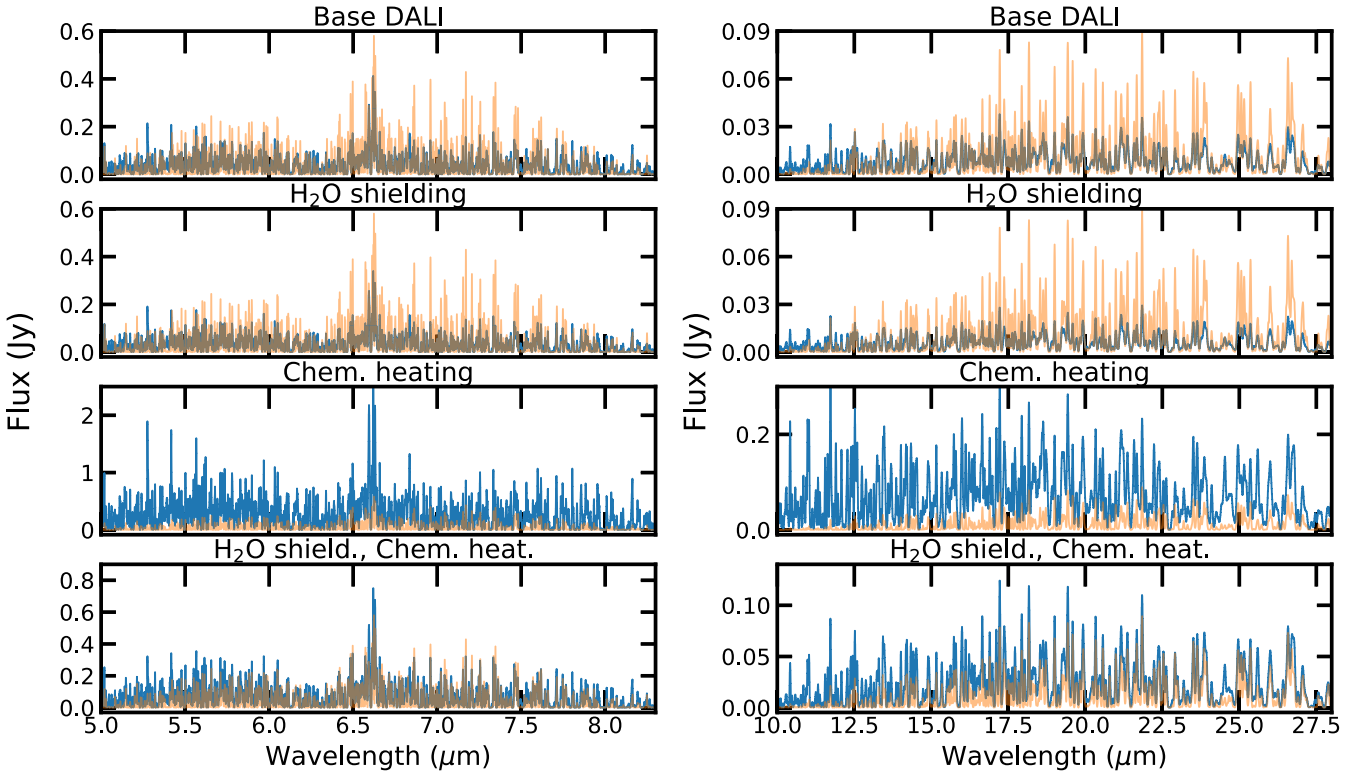


**Figure 3.** Water spectrum over most of the JWST-MIRI observable range for the thin model with a gas-to-dust ratio of $10^5$ in the surface layers (blue). The spectrum between 5 and 8 $\mu$m (left) is convolved to a resolving power of $R = 3000$, comparable to MIRI, the 10–28 $\mu$m spectrum on the right is convolved to an $R = 600$, to ease comparison with Spitzer spectra. The orange spectrum shows a water spectrum as computed from a typical slab model (Salyk et al. 2011), with an excitation temperature of 500 K and a $H_2O$ column of $3 \times 10^{18}$ cm$^{-2}$. In the Spitzer range, the model standard DALI and water UV-shielding models underpredict the $H_2O$ flux, except for the 10–12 $\mu$m regions. The extra heating models, however, overestimate the $H_2O$ flux, but the model with both extra heating and water UV-shielding fits the slab model better than the model with just water UV-shielding.

that water emission is not fully in LTE over the MIRI band, which we discuss in Section 4.2. Spectra for the different dust structures are discussed in Appendix C.

## 4. Discussion

### 4.1. Inner Disk Temperature Structure

The models clearly show that both the assumptions on chemical heating as well as the UV attenuation due to $H_2O$ have a strong impact on the predicted gas temperature and water abundance structure and resulting $H_2O$ spectra. Both should thus be considered in thermochemical models.

The main water-emitting layer ($H_2O$ columns of $\sim 10^{18}$ cm$^{-2}$ or more) is at high densities, $>10^{10}$ cm$^3$; as such in these layers, the very dense approximation of Glassgold & Najita (2015) should hold. Above this layer, the heating might be overestimated, as more energy can escape radiatively. This gas is not contributing to the emission so this is not critical for our conclusions.

The inclusion of water UV-shielding creates a region of the molecular layer that is shielded from UV photons by water and is also cooler. This layer starts below a water column of a few times $10^{18}$ cm$^{-2}$, corresponding to a $H_2$ column of 5–30 $\times$ $10^{22}$ cm$^{-2}$. This jump in temperature should be observable as cold lines, with a large column, and hotter lines coming from a smaller column in various inner disk tracers.

The rotational water spectra also contain information on the radial temperature gradient. The model water spectra are clearly not well captured by a single-temperature slab model. The relative brightness of the 10–14 $\mu$m lines compared to the slab model prediction is due to the higher temperatures at smaller radii. These boost the higher-excitation lines more than the falloff due to the emitting area. All our models, regardless of the inclusion of excess heating, show a power-law temperature–radius relation with a coefficient $q \sim -0.7$. A slab model fitting with this temperature profile will be necessary to properly describe the model and, most likely, the observed purely rotational lines of $H_2O$.

### 4.2. Water Excitation.

The vibrational band at 6.5 $\mu$m will require a similar radial rotational temperature profile to the pure rotational line. However, the comparison between the DALI model and slab spectra shows that this will not be enough, with the 6.5 $\mu$m being relatively weak. This mismatch in line brightness is due to the excitation of water. The highly excited rotational lines that dominate the spectrum longward of 10 $\mu$m are close to LTE in the emitting region (densities of $10^{11}$–$10^{12}$ cm$^{-3}$); however, at these densities, the vibrational band at 6.5 $\mu$m is not in LTE and is subthermally excited. Thermalization in the model happens at densities of $\sim 10^{13}$ cm$^{-3}$.

The excitation of water emission as measured with JWST-MIRI can thus be used to estimate the density of the emitting region. If the 6.5 $\mu$m band is weaker than expected from an LTE model fit to the 10–15 $\mu$m data, this is likely due to subthermal excitation of $H_2O$ and thus the (relatively) low density of the gas. This should be robust against uncertainties of the emitting area as the upper-level energies of the lines

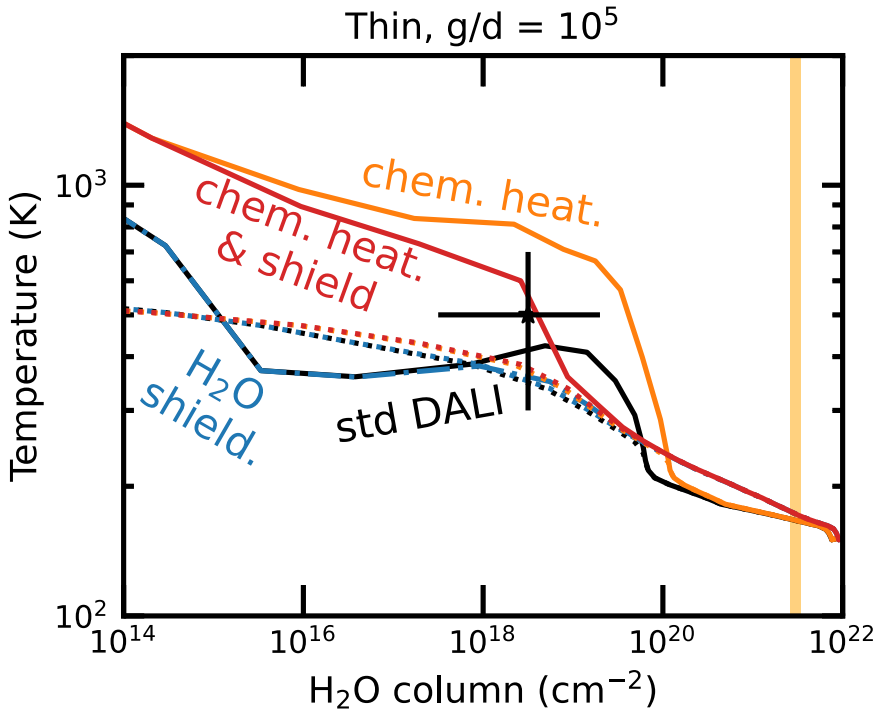


**Figure 4.** Gas temperature as a function of the cumulative vertical $H_2O$ column at the location of the midplane $H_2O$ ice line (0.4 au). The $H_2O$ column is a proxy for the location in the disk, the higher column being deeper into the disk. Due to the different abundance profiles in the models these $H_2O$ columns map to different total gas columns for the different models. Solid and dashed–dotted lines show the gas-temperature profiles, and the dotted lines show the dust temperature. The black star with the error bar gives the range of columns and excitation temperatures extracted from the Spitzer-IRS spectra (Salyk et al. 2011). The vertical orange line shows the approximate location where the dust becomes optically thick at 17 $\mu$m. Up to a column of $10^{17}$ cm$^{-2}$, the standard DALI and the water UV-shielding models are indistinguishable. At higher water columns, the shielding of $H_2O$ kicks in and heating by UV photons is suppressed.

around the center of the vibrational band (∼2300 K) are similar to the upper-level energies of the lines around 12 $\mu$m (∼2400 K).

### 4.3. The Inner Disk Water Reservoir

Infrared line observations only probe the surface layers of the disk. To extrapolate these observations to more general statements of the inner disk, both in terms of chemical complexity as well as in terms of midplane physical conditions, it is critical to understand what part of the disk we are actually probing with infrared spectra.

Figure 2 also illustrates the primary emission zone of water vapor at mid-IR wavelengths. The chemical models naturally and strongly predict a contained emission region that extends up to twice the midplane water snow-line radius. This agrees well with the analysis by Meijerink et al. (2009) and Blevins et al. (2016) that the water emission in T Tauri disks comes from a strongly radially contained region. With the variation in the observation data and in our model predictions, it is not possible to say if this containment is strong enough, or if containment within the radius of the water midplane snow line is necessary (as proposed by Meijerink et al. 2009; Bosman & Bergin 2021).

Vertically, most of the water emission is found arising from a thin hot layer where the gas-temperature structure is set by water UV-shielding. This zone is well above the dust optical surface. The layer probed by water infrared emission, and probably by many other inner disk tracers, is thus not set by the dust optical depth at the observed wavelength. Water lines with low Einstein $A$ coefficient lines or $H_2O$ isotopologues will be able to probe the deeper water abundance structure (see, e.g., Calahan et al. 2022). It is these deeper probing lines that will be necessary to constrain bulk disk surface properties, such as the C/O ratio and the gas-to-dust ratio.

However, our models do provide some information on the water column probed by observations, which is distinct from the total water column in the inner disk. Figure 4 shows the vertical gas and dust temperature structure as a function of the $H_2O$ column at the radius of the $H_2O$ midplane compared to the column density estimated via slab models of the water vapor emission in T Tauri systems observed by Spitzer (Salyk et al. 2011). Overall, our models find a much larger water column is present in the system at these radii (i.e., $\sim 10^{22}$ cm$^{-2}$ compared to few $\times 10^{18}$ cm$^{-2}$). However, what matters for the emission lines for transitions associated with mid-IR wavelengths is the column that is present at high temperature and the optical depth of these lines. Here we have two points to make. First, many of the strong water lines are optically thick at a column of $10^{18}$ cm$^{-2}$. Second, the gas temperature is rapidly falling below 400 K near a water column of a few $\times 10^{18}$ cm$^{-2}$. This effectively becomes the column traced by the mid-infrared lines. This is despite the fact that the total column exceeds this value (as first noted by Meijerink et al. 2009). This implies that the Spitzer spectra are only probing a small fraction of the observable inner disk water reservoir. In Calahan (2022), we illustrate that certain transitions of $H_2^{18}O$ can gain access to this reservoir. Regardless, detailed models will be needed to match observational data and infer the underlying hidden $H_2O$ content.

### 4.4. M-dwarf and Herbig Ae Disks

The model discussed so far is representative of a disk around a young, solar-mass star. However, many of the objects to be observed will have a far different mass range and spectral energy distributions. To capture some of these effects, we looked at two additional model runs, one around an M dwarf (Hauschildt et al. 1999; Herczeg et al. 2004; M3, 3300 K, 0.1 $L_\odot$, $L_{<200\mathrm{nm}} = 10^{-3} L_\odot$) and Herbig Ae (A1, 9300 K, 14 $L_\odot$, $L_{<200\mathrm{nm}} = 0.8 L_\odot$, HD 163296 in Zhang et al. 2021). The X-ray luminosity is taken to be $10^{29}$ erg s$^{-1}$ for both models. The disk structures are identical to those from Table 1, except that the sublimation radius is scaled to 0.022 and 0.3 au for the M-dwarf and Herbig Ae disks, respectively.

The M-dwarf disk water spectra in general are well described by the T Tauri water spectra linearly scaled down with the stellar luminosity, especially for the models with a gas-to-dust ratio of $10^4$ in the disk surface layer. For a gas-to-dust ratio of $10^5$, the models with extra chemical heating were about a factor of 2 brighter than would be expected from a linearly scaled down T Tauri model.

The Herbig Ae disk water spectra are across the board brighter than a T Tauri model linearly scaled up with luminosity, likely due to the higher UV-to-total luminosity ratio of the Herbig Ae stellar spectrum. This causes a higher contrast between midplane dust temperature and surface layer gas temperature, leading to stronger water emission relative to the total stellar luminosity. This effect is supercharged in models with a gas-to-dust ratio of $10^5$ that include chemical heating. While the total luminosity increases by a factor of 10, the water-line fluxes between 10 and 28 $\mu$m increase by more than a factor of 100.

For the Herbig Ae disks, these stronger line fluxes (and stronger line-to-continuum ratios) are counter to the observations, where water is not detected toward a majority of sources (Pontoppidan et al. 2010; Antonellini et al. 2016). This implies that there is a fundamental difference in the disk structures between T Tauri and Herbig Ae disks. This might be related lower gas-to-dust ratios in the surface layers of the Herbig Ae disk compared to T Tauris, leading to low contrast between water lines and the continuum (Antonellini et al. 2016) or to the inferred puffed-up inner rims, which could radially constrain the infrared line emission, which is also seen in the CO rovibrational lines (Dullemond & Monnier 2010; Bosman et al. 2019).

## 5. Conclusions

We have studied the impact of water UV-shielding and chemical heating on the emission of water in the mid-infrared. We find that the inclusion of water UV-shielding and extra chemical heating significantly impacts the temperature in the water-line-emitting layer. Both are required to match the observed spectra. The extra chemical heating raises the temperature at the top of the water-emitting layer to the observed values. Water UV-shielding cools down the disk below this region by excluding UV photons. This limits the $H_2O$ column that can emit to the observed column values.

This results in the models having a large region above the dust mid-infrared photosphere that contains colder water that does not significantly contribute to the observed spectrum. This leads to a one to two order of magnitude mismatch between the theoretically observable water column and the water column implied by the spectrum. This reservoir might be visible with select $H_2^{18}O$ lines. Radially, the $H_2O$-emitting region is naturally confined by the chemistry.

Model spectra are not fully captured by a single LTE slab model. High upper-level energy lines generally originate from a smaller but hotter emitting region, while the vibrational emission around 6.5 $\mu$m comes from vibrationally subthermally excited $H_2O$, while the rotational transitions are generally in LTE. This suggests that future observations from JWST could extract both density and temperature within emitting layers.

The authors thank the referee for a constructive report that improved the quality of the paper. We also thank Benoît Tabone and Stephanie Cazaux for the useful discussion on $H_2$ formation. A.D.B. and E.A.B. acknowledge support from NSF grant#1907653 and NASA grant XRP 80NSSC20K0259.

*Software:* Astropy (Astropy Collaboration et al. 2013, 2018), SciPy (Virtanen et al. 2020), NumPy (Van Der Walt et al. 2011), Matplotlib (Hunter 2007), DALI (Bruderer et al. 2012; Bruderer 2013).

## Appendix A
## Reactions Added to the Network

In our model, $H_2$ formation in warm gas has to be increased to create water abundances high up in the disk (Glassgold et al. 2009). This is facilitated by increasing the chemisorption binding energy from 10,000 to 30,000 K within the formalism of Cazaux & Tielens (2002, 2004). With these assumptions, the dust temperature allows $H_2$ to form on the grains from ~300 to ~900 K in line with experiments of $H_2$ formation in the lab on various surfaces (Wakelam et al. 2017, Cazaux, private communication); this is in line with assumptions made by Ádámkovics et al. (2014). As densities in the inner disk can reach $10^{12}$ cm$^{-3}$ in the UV-penetrated layers, we also included a number of 3 body reactions. Notably, this included the

$$\mathrm{H} + \mathrm{H} + \mathrm{H} \longrightarrow \mathrm{H_2} + \mathrm{H} \tag{A1}$$

reaction, which increases the $H_2$ formation rate at higher density. A full list of the reactions and their coefficients can be seen in Table 2. Reactions are taken from the network used in Walsh et al. (2015).

**Table 2**
Reactions with Reaction Coefficients ($k = a \times (T/300)^b \exp(-c/T)$)

| Reaction | $a$ | $b$ | $c$ (K) | Reaction | $a$ | $b$ | $c$ (K) |
|---|---|---|---|---|---|---|---|
| $H + H + H \longrightarrow H_2 + H$ | 1.422(−32) | −0.2 | 0 | | | | |
| $H + H + H \longrightarrow H_2 + H$ | 1.150(−32) | −0.5 | 0 | | | | |
| $H + H + H_2 \longrightarrow H_2 + H_2$ | 9.100(−33) | −0.6 | 0 | | | | |
| $H_2 + e^- \longrightarrow H + H + e^-$ | 3.220(−09) | −0.3 | 1.020(5) | | | | |
| $C + H_2 + H \longrightarrow CH_2 + H$ | 6.900(−32) | 0 | 0 | $C + H_2 + H_2 \longrightarrow CH_2 + H_2$ | 6.900(−32) | 0 | 0 |
| $CH + H_2 + H \longrightarrow CH_3 + H$ | 5.100(−30) | −1.6 | 0 | $CH + H_2 + H_2 \longrightarrow CH_3 + H_2$ | 5.100(−30) | −1.6 | 0 |
| $CH_3 + H + H \longrightarrow CH_4 + H$ | 6.300(−29) | −1.8 | 0 | $CH_3 + H + H_2 \longrightarrow CH_4 + H_2$ | 6.300(−29) | −1.8 | 0 |
| $O + H + H \longrightarrow OH + H$ | 4.330(−32) | −1.0 | 0 | $O + H + H_2 \longrightarrow OH + H_2$ | 4.330(−32) | −1.0 | 0 |
| $OH + H + H \longrightarrow H_2O + H$ | 2.600(−31) | −2.0 | 0 | $OH + H + H_2 \longrightarrow H_2O + H_2$ | 2.600(−31) | −2.0 | 0 |
| $NH_2 + H + H \longrightarrow NH_3 + H$ | 3.010(−30) | 0 | 0 | $NH_2 + H + H_2 \longrightarrow NH_3 + H_2$ | 3.010(−30) | 0 | 0 |
| $O + O + H \longrightarrow O_2 + H$ | 5.210(−35) | 0 | −9.000(2) | $O + O + H_2 \longrightarrow O_2 + H_2$ | 5.210(−35) | 0 | −9.000(2) |
| $N + N + H \longrightarrow N_2 + H$ | 1.380(−33) | 0 | −5.030(2) | $N + N + H_2 \longrightarrow N_2 + H_2$ | 1.380(−33) | 0 | −5.030(2) |
| $CO + H + H \longrightarrow HCO + H$ | 6.300(−35) | 0.2 | 0 | $CO + H + H_2 \longrightarrow HCO + H_2$ | 6.300(−35) | 0.2 | 0 |
| $CN + H + H \longrightarrow HCN + H$ | 8.500(−30) | −2.2 | 5.670(2) | $CN + H + H_2 \longrightarrow HCN + H_2$ | 8.500(−30) | −2.2 | 5.670(2) |
| $CO + O + H \longrightarrow CO_2 + H$ | 1.700(−33) | 0 | 1.510(3) | $CO + O + H_2 \longrightarrow CO_2 + H_2$ | 1.700(−33) | 0 | 1.510(3) |
| $H_2 + H \longrightarrow H + H + H$ | 1.000(−08) | 0 | 8.410(4) | $H_2 + H_2 \longrightarrow H + H + H_2$ | 1.000(−08) | 0 | 8.410(4) |
| $CH + H \longrightarrow C + H + H$ | 6.000(−09) | 0 | 4.020(4) | $CH + H_2 \longrightarrow C + H + H_2$ | 6.000(−09) | 0 | 4.020(4) |
| $CH_2 + H \longrightarrow C + H_2 + H$ | 5.000(−10) | 0 | 3.260(4) | $CH_2 + H_2 \longrightarrow C + H_2 + H_2$ | 5.000(−10) | 0 | 3.260(4) |
| $CH_2 + H \longrightarrow CH + H + H$ | 1.560(−08) | 0 | 4.488(4) | $CH_2 + H_2 \longrightarrow CH + H + H_2$ | 1.560(−08) | 0 | 4.488(4) |
| $CH_3 + H \longrightarrow CH_2 + H + H$ | 1.700(−08) | 0 | 4.560(4) | $CH_3 + H_2 \longrightarrow CH_2 + H + H_2$ | 1.700(−08) | 0 | 4.560(4) |
| $CH_3 + H \longrightarrow CH + H_2 + H$ | 1.100(−08) | 0 | 4.280(4) | $CH_3 + H_2 \longrightarrow CH + H_2 + H_2$ | 1.100(−08) | 0 | 4.280(4) |
| $CH_4 + H \longrightarrow CH_3 + H + H$ | 7.500(−07) | 0 | 4.570(4) | $CH_4 + H_2 \longrightarrow CH_3 + H + H_2$ | 7.500(−07) | 0 | 4.570(4) |
| $NH_3 + H \longrightarrow NH + H_2 + H$ | 3.100(−08) | 0 | 4.686(4) | $NH_3 + H_2 \longrightarrow NH + H_2 + H_2$ | 3.100(−08) | 0 | 4.686(4) |
| $NH_3 + H \longrightarrow NH_2 + H + H$ | 4.170(−08) | 0 | 4.720(4) | $NH_3 + H_2 \longrightarrow NH_2 + H + H_2$ | 4.170(−08) | 0 | 4.720(4) |
| $OH + H \longrightarrow O + H + H$ | 6.000(−09) | 0 | 5.090(4) | $OH + H_2 \longrightarrow O + H + H_2$ | 6.000(−09) | 0 | 5.090(4) |
| $H_2O + H \longrightarrow OH + H + H$ | 5.800(−09) | 0 | 5.290(4) | $H_2O + H_2 \longrightarrow OH + H + H_2$ | 5.800(−09) | 0 | 5.290(4) |
| $O_2 + H \longrightarrow O + O + H$ | 6.000(−09) | 0 | 5.230(4) | $O_2 + H_2 \longrightarrow O + O + H_2$ | 6.000(−09) | 0 | 5.230(4) |
| $CO + H \longrightarrow C + O + H$ | 1.480(−04) | −3.1 | 1.290(5) | $CO + H_2 \longrightarrow C + O + H_2$ | 1.480(−04) | −3.1 | 1.290(5) |
| $HCO + H \longrightarrow CO + H + H$ | 6.600(−11) | 0 | 7.820(3) | $HCO + H_2 \longrightarrow CO + H + H_2$ | 6.600(−11) | 0 | 7.820(3) |
| $H_2CO + H \longrightarrow HCO + H + H$ | 2.450(−08) | 0 | 3.805(4) | $H_2CO + H_2 \longrightarrow HCO + H + H_2$ | 2.450(−08) | 0 | 3.805(4) |
| $H_2CO + H \longrightarrow CO + H_2 + H$ | 1.420(−08) | 0 | 3.210(4) | $H_2CO + H_2 \longrightarrow CO + H_2 + H_2$ | 1.420(−08) | 0 | 3.210(4) |
| $CN + H \longrightarrow C + N + H$ | 4.200(−10) | 0 | 7.100(4) | $CN + H_2 \longrightarrow C + N + H_2$ | 4.200(−10) | 0 | 7.100(4) |
| $HCN + H \longrightarrow CN + H + H$ | 2.150(−04) | −2.6 | 6.280(4) | $HCN + H_2 \longrightarrow CN + H + H_2$ | 2.150(−04) | −2.6 | 6.280(4) |
| $NO + H \longrightarrow N + O + H$ | 1.600(−09) | 0 | 7.460(4) | $NO + H_2 \longrightarrow N + O + H_2$ | 1.600(−09) | 0 | 7.460(4) |
| $SO_2 + H \longrightarrow SO + O + H$ | 4.200(−10) | 0 | 5.540(4) | $SO_2 + H_2 \longrightarrow SO + O + H_2$ | 4.200(−10) | 0 | 5.540(4) |

**Note.** $x(y) \equiv x \times 10^y$; $a$ is in units of $cm^3\ s^{-1}$ or $cm^6\ s^{-1}$ for two- and three-body reactions, respectively.

## Appendix B
## Disk Structure Variations

Figure 5 shows the gas temperature and water abundance for a thick model with a surface layer gas-to-dust ratio of $10^5$. The more puffed-up structure intercepts more stellar flux, leading to a warmer disk in general. Pushing out the midplane water-ice line as well as the water-emitting region. Furthermore, the UV-heated molecular and water-emitting layers are higher up in the disk.

Apart from the upward and outward scaling, there are no significant differences in the water abundance structure, the gap in the water abundance at large radii also appears in the thicker model. As in the thin model, the inclusion of water UV-shielding strongly increases the abundance of this region, making water the dominant water carrier in the entire inner disk region.

Increasing the amount of small dust has the main effect of cooling down the surface layers. Specifically, the UV-heated layer shrinks radially and moves upward. This is mostly caused by the more efficient gas-grain cooling. This directly affects the water abundance structure. The water is less extended in the surface layers due to the lower temperatures. This naturally causes a smaller emitting area for the water.

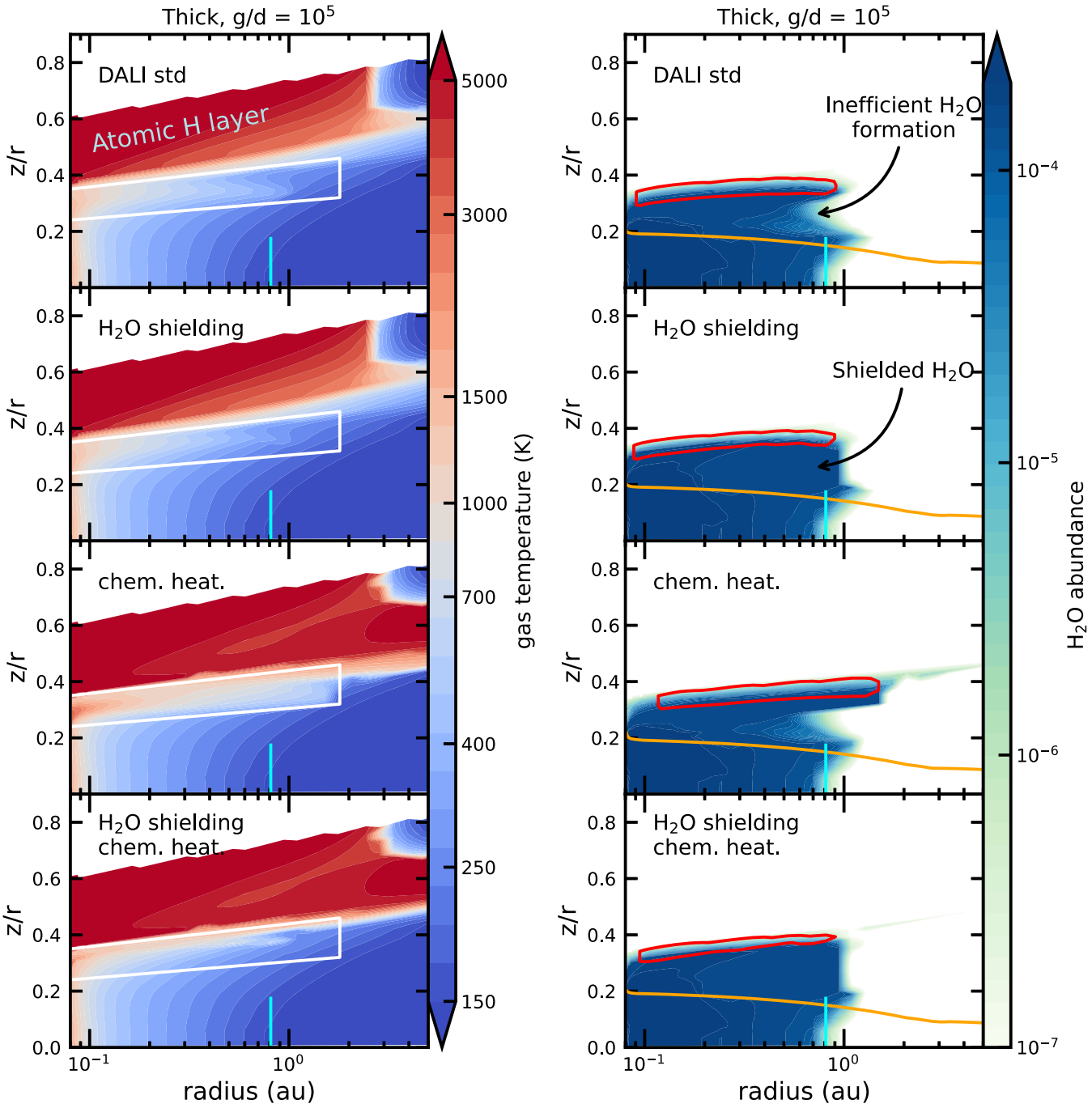


**Figure 5.** Same as Figure 2 but for the thick model with a surface layer gas-to-dust ratio of $10^5$.

## Appendix C
## Spectra for Disk Variations

Figures 6, 7, and 8 show the water spectra for three structures in Figure 1; the final spectrum is in Figure 3 in the main text. The behavior of the spectra with extra chemical heating as well as with water UV-shielding is consistent over the different structures. This implies that our observations are robust to disk structure.

The water-line flux is increased with increased disk scale height as well as with increased gas-to-dust ratios. Lower amounts of dust allow for more UV photons to penetrate the $H_2O$-emitting layer, increasing the gas temperature. In the more puffed-up models, the $H_2O$-emitting layer is present at slightly higher temperatures as lower densities suppress gas cooling.

For the models that include water UV-shielding, it is clear that the thin model with a $10^4$ surface gas-to-dust ratio undershoots the slab model and that the thick model with a $10^4$ surface gas-to-dust ratio only just matches the flux when extra chemical heating is included. As such, a surface layer gas-to-dust ratio $>10^4$ or a very thick disk ($h/r > 0.1$ at 1 au) is necessary to reproduce the water spectra.

The model with excess chemical heating absorbs most of the incident UV photon energy and deposits it in the gas. Increasing the gas heating beyond this needs a different energy

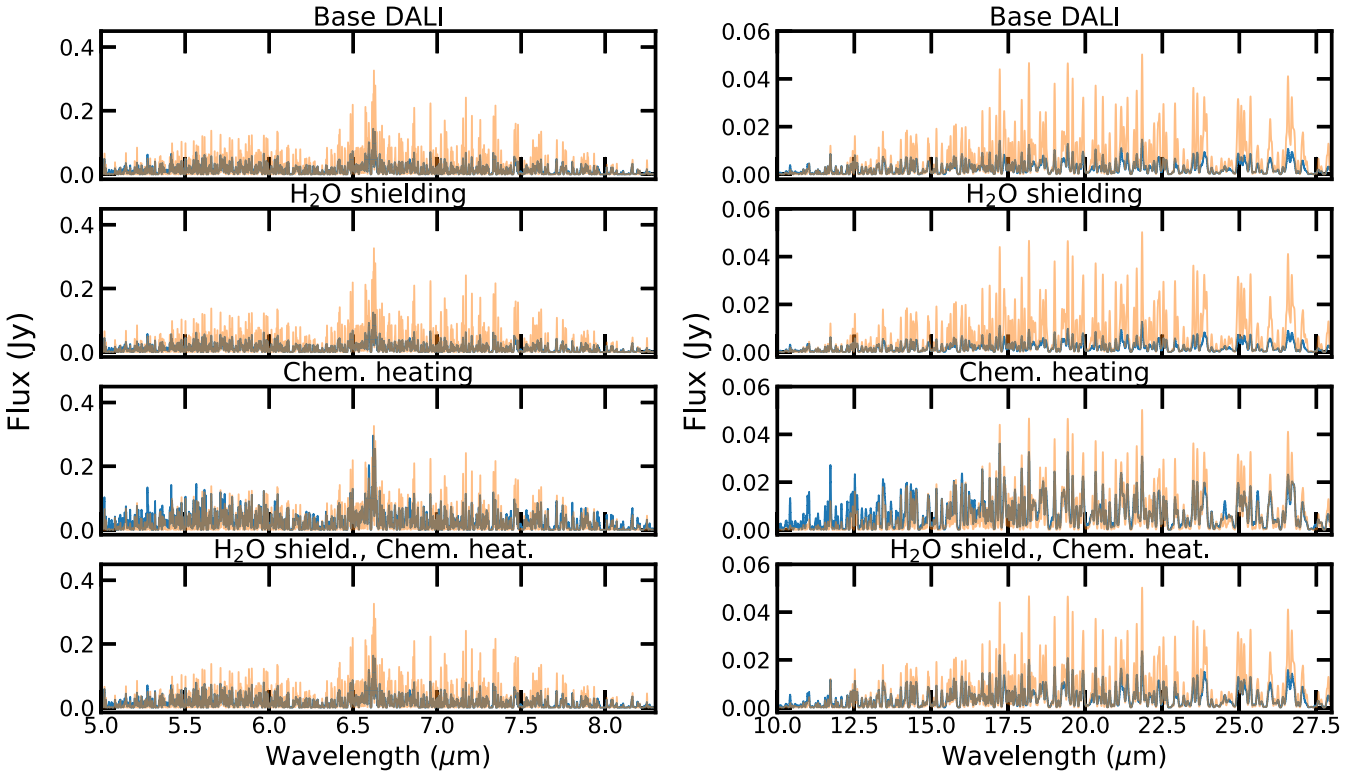


**Figure 6.** Same as Figure 3 but for the thin model with a surface layer gas-to-dust ratio of $10^4$.

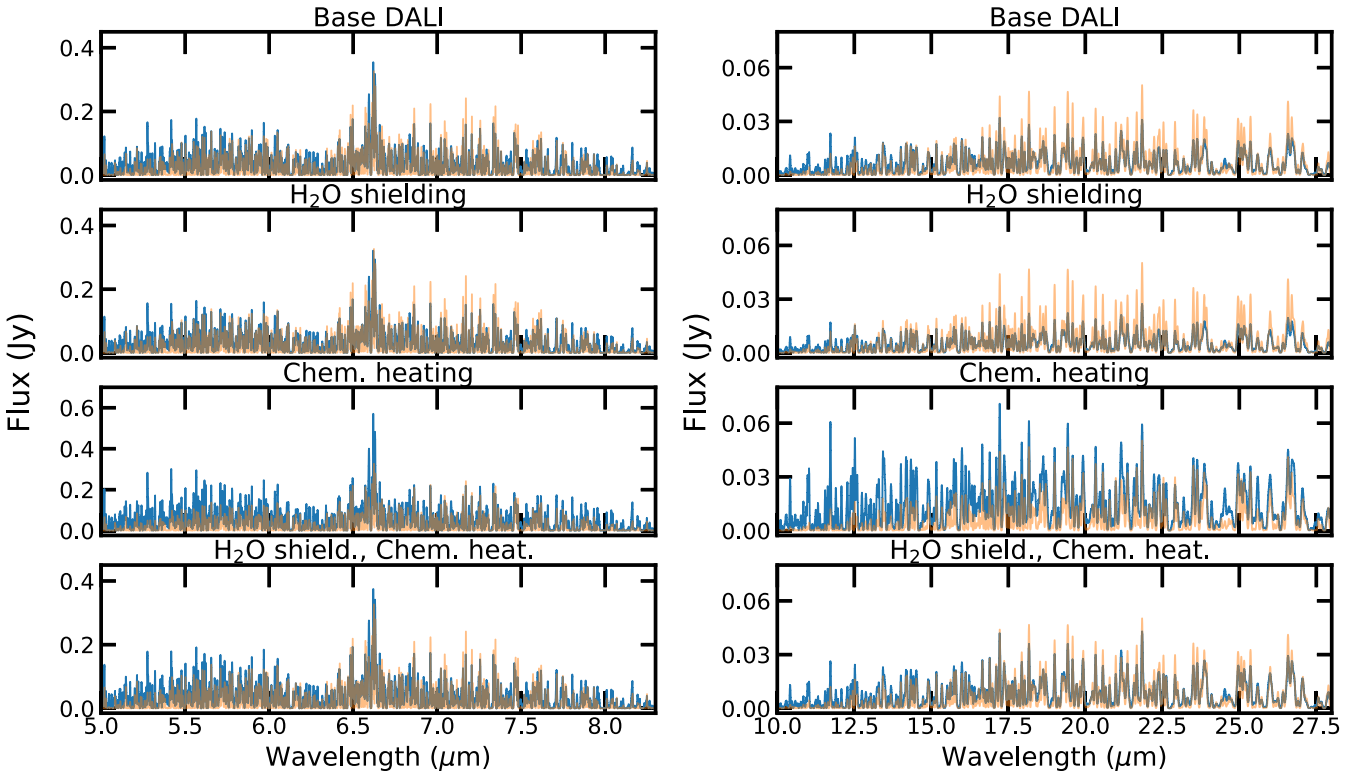


**Figure 7.** Same as Figure 3 but for the thick model with a surface layer gas-to-dust ratio of $10^4$.

source than the central star. One obvious candidate would be heating from accreting gas (e.g., Glassgold et al. 2004). As the temperature is driven by the local heating due to stellar photon and gas cooling, local heating is going to be far more effective in increasing the temperature than heating near the disk midplane. The inclusion of accretion heating would allow for lower gas-to-dust ratios in the disk surface to still reproduce the observed spectra. A scenario with a lower gas-to-dust ratio but

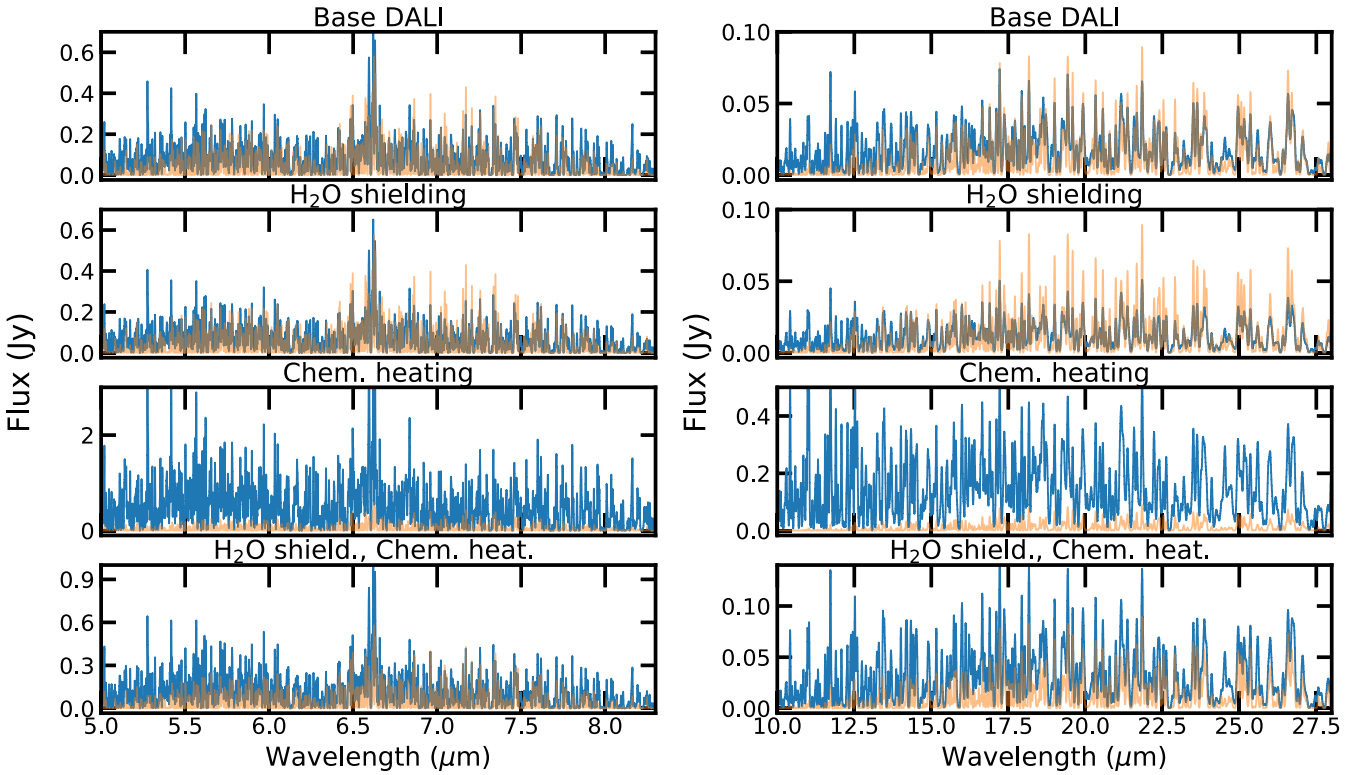


**Figure 8.** Same as Figure 3 but for the thick model with a surface layer gas-to-dust ratio of $10^5$.

with accretion heating to compensate would be hard to distinguish from a high gas-to-dust ratio with no accretion heating in the water emission. The lack of a deeper, colder visible gas reservoir could be seen in various less abundant species and help distinguish among these scenarios.

## ORCID iDs

Arthur D. Bosman https://orcid.org/0000-0003-4001-3589
Edwin A. Bergin https://orcid.org/0000-0003-4179-6394
Jenny Calahan https://orcid.org/0000-0002-0150-0125

## References

Ádámkovics, M., Glassgold, A. E., & Najita, J. R. 2014, ApJ, 786, 135
Ádámkovics, M., Najita, J. R., & Glassgold, A. E. 2016, ApJ, 817, 82
Anderson, D. E., Blake, G. A., Cleeves, L. I., et al. 2021, ApJ, 909, 55
Antonellini, S., Banzatti, A., Kamp, I., Thi, W. F., & Woitke, P. 2020, A&A, 637, A29
Antonellini, S., Kamp, I., Lahuis, F., et al. 2016, A&A, 585, A61
Astropy Collaboration, Price-Whelan, A. M., Sipőcz, B. M., et al. 2018, AJ, 156, 123
Astropy Collaboration, Robitaille, T. P., Tollerud, E. J., et al. 2013, A&A, 558, A33
Banzatti, A., Meyer, M. R., Bruderer, S., et al. 2012, ApJ, 745, 90
Barber, R. J., Tennyson, J., Harris, G. J., & Tolchenov, R. N. 2006, MNRAS, 368, 1087
Bethell, T., & Bergin, E. 2009, Sci, 326, 1675
Birnstiel, T., Dullemond, C. P., Zhu, Z., et al. 2018, ApJL, 869, L45
Blevins, S. M., Pontoppidan, K. M., Banzatti, A., et al. 2016, ApJ, 818, 22
Bosman, A. D., & Banzatti, A. 2019, A&A, 632, L10
Bosman, A. D., Banzatti, A., Bruderer, S., et al. 2019, A&A, 631, A133
Bosman, A. D., & Bergin, E. A. 2021, ApJL, 918, L10
Bosman, A. D., Bergin, E. A., Calahan, J., & Duval, S. E. 2022, ApJL, submitted
Bosman, A. D., Bruderer, S., & van Dishoeck, E. F. 2017, A&A, 601, A36
Brown, J. M., Pontoppidan, K. M., van Dishoeck, E. F., et al. 2013, ApJ, 770, 94
Bruderer, S. 2013, A&A, 559, A46
Bruderer, S., Harsono, D., & van Dishoeck, E. F. 2015, A&A, 575, A94
Bruderer, S., van Dishoeck, E. F., Doty, S. D., & Herczeg, G. J. 2012, A&A, 541, A91
Calahan, J., Bergin, E. A., & Bosman, A. D. 2022, ApJL, submitted
Carr, J. S., & Najita, J. R. 2008, Sci, 319, 1504
Cazaux, S., & Tielens, A. G. G. M. 2002, ApJL, 575, L29
Cazaux, S., & Tielens, A. G. G. M. 2004, ApJ, 604, 222
Chan, W. F., Cooper, G., & Brion, C. E. 1993, CP, 178, 387
Dionatos, O., Woitke, P., Güdel, M., et al. 2019, A&A, 625, A66
Dullemond, C. P., & Monnier, J. D. 2010, ARA&A, 48, 205
Faure, A., & Josselin, E. 2008, A&A, 492, 257
Fillion, J. H., Dulieu, F., Baouche, S., et al. 2003, JPhB, 36, 2767
Fillion, J. H., Ruiz, J., Yang, X. F., et al. 2004, JChPh, 120, 6531
Fulton, B. J., Rosenthal, L. J., Hirsch, L. A., et al. 2021, ApJS, 255, 14
Glassgold, A. E., Meijerink, R., & Najita, J. R. 2009, ApJ, 701, 142
Glassgold, A. E., Najita, J., & Igea, J. 2004, ApJ, 615, 972
Glassgold, A. E., & Najita, J. R. 2015, ApJ, 810, 125
Hauschildt, P. H., Allard, F., Ferguson, J., Baron, E., & Alexander, D. R. 1999, ApJ, 525, 871
Heays, A. N., Bosman, A. D., & van Dishoeck, E. F. 2017, A&A, 602, A105
Herczeg, G. J., Wood, B. E., Linsky, J. L., Valenti, J. A., & Johns-Krull, C. M. 2004, ApJ, 607, 369
Hunter, J. D. 2007, CSE, 9, 90
Madhusudhan, N. 2019, ARA&A, 57, 617
Meijerink, R., Pontoppidan, K. M., Blake, G. A., Poelman, D. R., & Dullemond, C. P. 2009, ApJ, 704, 1471
Mota, R., Parafita, R., Giuliani, A., et al. 2005, CPL, 416, 152
Najita, J., Carr, J. S., & Mathieu, R. D. 2003, ApJ, 589, 931
Pontoppidan, K. M., & Blevins, S. M. 2014, FaDi, 169, 49
Pontoppidan, K. M., Salyk, C., Bergin, E. A., et al. 2014, in Protostars and Planets VI, ed. H. Beuther et al. (Tucson, AZ: Univ. Arizona Press), 363
Pontoppidan, K. M., Salyk, C., Blake, G. A., et al. 2010, ApJ, 720, 887
Salyk, C., Pontoppidan, K. M., Blake, G. A., Najita, J. R., & Carr, J. S. 2011, ApJ, 731, 130
Schindhelm, R., France, K., Herczeg, G. J., et al. 2012, ApJL, 756, L23
Tennyson, J., Zobov, N. F., Williamson, R., Polyansky, O. L., & Bernath, P. F. 2001, JPCRD, 30, 735
Thi, W. F., Hocuk, S., Kamp, I., et al. 2020, A&A, 634, A42
Van Der Walt, S., Colbert, S. C., & Varoquaux, G. 2011, CSE, 13, 22

van Terwisga, S. E., Hacar, A., van Dishoeck, E. F., Oonk, R., & Portegies Zwart, S. 2022, arXiv:2202.11057
Virtanen, P., Gommers, R., Oliphant, T. E., et al. 2020, NatMe, 17, 261
Wakelam, V., Bron, E., Cazaux, S., et al. 2017, MolAs, 9, 1
Walsh, C., Nomura, H., & van Dishoeck, E. 2015, A&A, 582, A88
Woitke, P., Kamp, I., Antonellini, S., et al. 2019, PASP, 131, 064301
Woitke, P., Min, M., Thi, W. F., et al. 2018, A&A, 618, A57
Zhang, K., Booth, A. S., Law, C. J., et al. 2021, ApJS, 257, 5